Highly Reproducible Sn-Based Hybrid Perovskite Solar Cells with 9% Efficiency

Shao, Shuyan; Liu, Jian; Portale, Giuseppe; Fang, Hong-Hua; Blake, Graeme R.; ten Brink, Gert H.; Koster, L. Jan Anton; Loi, Maria Antonietta

Published in:
Advanced Energy Materials

DOI:
10.1002/aenm.201702019

Publication date:
2018

ADVANCED ENERGY MATERIALS

www.advenergymat.de

Highly Reproducible Sn-Based Hybrid Perovskite Solar Cells with 9% Efficiency

*Shuyan Shao, Jian Liu, Giuseppe Portale, Hong-Hua Fang, Graeme R. Blake, Gert H. ten Brink, L. Jan Anton Koster, and Maria Antonietta Loi**

The low power conversion efficiency (PCE) of tin-based hybrid perovskite solar cells (HPSCs) is mainly attributed to the high background carrier density due to a high density of intrinsic defects such as Sn vacancies and oxidized species (Sn^{4+}) that characterize Sn-based HPSCs. Herein, this study reports on the successful reduction of the background carrier density by more than one order of magnitude by depositing near-single-crystalline formamidinium tin iodide ($FASnI_3$) films with the orthorhombic *a*-axis in the out-of-plane direction. Using these highly crystalline films, obtained by mixing a very small amount (0.08 M) of layered (2D) Sn perovskite with 0.92 M (3D) $FASnI_3$, for the first time a PCE as high as 9.0% in a planar p–i–n device structure is achieved. These devices display negligible hysteresis and light soaking, as they benefit from very low trap-assisted recombination, low shunt losses, and more efficient charge collection. This represents a 50% improvement in PCE compared to the best reference cell based on a pure $FASnI_3$ film using SnF_2 as a reducing agent. Moreover, the 2D/3D-based HPSCs show considerable improved stability due to the enhanced robustness of the perovskite film compared to the reference cell.

Three dimensional (3D) perovskite materials with an ABX_3 structure (where A is either an organic or an inorganic cation, B is a divalent metal cation, and X is a halide anion) have demonstrated superb properties as light absorbers in photovoltaic devices. Thanks to the intensive research efforts of a large scientific community over the past 7 years, lead (Pb)-based hybrid perovskite solar cells (HPSCs) have achieved an impressive (up to 22%) power conversion efficiency (PCE).[1] At the same time, researchers have also demonstrated progress in improving the thermal and photostability of this kind of solar cell by using more stable precursors and robust hole/electron transport layers.[2–5] Despite these outstanding achievements, the toxicity of lead causes concerns about the possible large-scale utilization of this new type of solar cell.

Therefore, attention has recently turned towards lead-free HPSCs with the idea of replacing lead by less toxic metals. Among the various alternatives to lead, tin (Sn) has great potential as the Sn-based hybrid perovskites display excellent optical and electrical properties such as high absorption coefficients, small exciton binding energies, and high charge carrier mobilities.[6–11] However, the record PCE of tin-based HPSCs has remained at about 6% for more than 3 years since the very first reports by the groups of Snaith and Kanatzidis, who reported methylammonium tin halide ($MASnI_3$ and $MASnI_{3-x}Br_x$) solar cells with an n–i–p structure and TiO_2 mesoporous scaffold in 2014, which showed PCE of 6.4% and 5.73%, respectively.[12,13] In an attempt to improve the PCE, research efforts have been directed towards optimization of the tin-perovskite film morphology, tuning the film composition, use of a reducing agent, and modification of the device structure.[14–21]

The main challenges for further improving the PCE lie in preventing the easy formation of Sn vacancies due to their small formation energy and the fast oxidation of divalent Sn^{2+} into more stable Sn^{4+}. This causes high levels of self-p-doping in Sn-based perovskite films, with consequent severe recombination losses for charge carriers. Therefore, attempts to reduce the background carrier (hole) density have been made by incorporating SnF_2 into such films to fill tin vacancies and suppress oxidation of Sn^{2+}.[14–17] For example, Mathews and co-workers reported the use of cesium tin iodide ($CsSnI_3$) and formamidinium tin iodide ($FASnI_3$) as light absorbers in an

Dr. S. Shao, Dr. J. Liu, Dr. H.-H. Fang, Dr. L. J. A. Koster, Prof. M. A. Loi
Photophysics and OptoElectronics
Zernike Institute for Advanced Materials
University of Groningen
Nijenborgh 4, 9747 AG Groningen, The Netherlands
E-mail: m.a.loi@rug.nl

Dr. G. Portale
Macromolecular Chemistry and New Polymeric Material
Zernike Institute for Advanced Materials
University of Groningen
Nijenborgh 4, 9747 AG Groningen, The Netherlands

Dr. G. R. Blake
Solid State Materials for Electronics
Zernike Institute for Advanced Materials
University of Groningen
Nijenborgh 4, 9747 AG Groningen, The Netherlands

Dr. G. H. ten Brink
Nanostructured Materials and Interfaces
Zernike Institute for Advanced Materials
University of Groningen
Nijenborgh 4, 9747 AG Groningen, The Netherlands

The ORCID identification number(s) for the author(s) of this article can be found under https://doi.org/10.1002/aenm.201702019.

DOI: 10.1002/aenm.201702019

n–i–p device structure (with the n-type layer being mesoscopic) and demonstrated a PCE of ≈2% using tin fluoride (SnF_2) as a reducing agent.[14] Later, Seok and co-workers demonstrated a PCE of 4.8% by improving the $FASnI_3$ film morphology using pyrazine to form a complex with SnF_2 and slowing down the thin film crystallization.[15] More recently, Yan and co-workers reported a PCE of 6.22% in an inverted p–i–n planar device structure.[16]

However, an excess of SnF_2 deteriorates the perovskite film morphology and the device performance,[14–16] implying that the SnF_2 concentration must be kept low with the consequence that the background carrier density in these HPSCs is still too high to achieve equivalent performance to the lead-based perovskites. Therefore, it is necessary to develop new and more effective strategies to further reduce the background carrier density and improve the device performance of tin-based HPSCs.

Such alternative strategies have been explored by only a handful of research groups. Kanatzidis and co-workers showed that processing the perovskite film containing SnF_2 under a reducing vapor atmosphere helps to reduce the hole carrier density in $MASnI_3$ films.[19] Unlike SnF_2, the reducing vapor protects the tin-perovskite film from oxidation during the film-forming process but is absent in the HPSCs themselves. The best device created using this method, however, displayed a PCE of around 3.8%, i.e., inferior to previously reported devices processed without a reducing atmosphere. Hatton and co-workers reported that adding an excess of tin chloride ($SnCl_2$) and tin iodide (SnI_2) to $CsSnI_3$ films improves both the stability and PCE of the corresponding solar cells, which displayed a PCE of ≈3%.[20,21] Just before the submission of this manuscript, Zhao et al. reported tin-based HPSCs with a PCE of 8.12% by using mixed cation tin perovskite ($FA_{0.75}MA_{0.25}SnI_3$) as light harvesting layer.[22] Despite the relatively high efficiency, the resistance to moisture of $FA_{0.75}MA_{0.25}SnI_3$-based HPSCs should be quite limited because of the hydrophilic FA^+ and MA^+ cations.

A lesson learned from lead-based perovskite is that low-dimensional perovskite formed by replacing the small hydrophilic cations with much bulkier organic ones can help to improve the stability of the HPSCs upon exposure to moisture.[23–25] Unlike the comprehensive studies on lead-based perovskite, only two papers about tin-based HPSCs using low-dimensional perovskite such as $(CH_3(CH_2)_3NH_3)_2(CH_3NH_3)_{n-1}Sn_nI_{3n+1}$ and $PEA_2FA_{n-1}Sn_nI_{3n+1}$ (n is the number of the inorganic SnI_6 octahedra layers encapsulated by the PEA^+ ($PEA = C_6H_5(CH_2)_2NH_3^+$) double layer, the increase (decrease) in n value means increase (decrease) in the dimension; $n = \infty$ 3D perovskite, $n = 1$ 2D perovskite) were published during the preparation of this manuscript.[26,27] In both papers, the PCE of the tin-based HPSCs are still lower than 6%. Cao et al. reported a PCE of 2.5% by using $(CH_3(CH_2)_3NH_3)_2(CH_3NH_3)_3Sn_4I_{13}$ ($n = 4$) as light harvesting layer.[26] Ning and co-workers reported a PCE of 5.9% using $PEA_2FA_8Sn_9I_{28}$ ($n = 9$) as light harvesting layer.[27] For the low-dimensional tin-based perovskite family $(CH_3(CH_2)_3NH_3)_2(CH_3NH_3)_{n-1}Sn_nI_{3n+1}$ and $PEA_2FA_{n-1}Sn_nI_{3n+1}$, how the device using tin perovskite with lower content of bulkier organic cations ($\infty > n > 5$ for $(CH_3(CH_2)_3NH_3)_2(CH_3NH_3)_{n-1}Sn_nI_{3n+1}$, $\infty > n > 9$ for $PEA_2FA_{n-1}Sn_nI_{3n+1}$) as light harvesting layer behaves, remains an open question.

Herein, for the first time, we report a PCE as high as 9% for tin-based HPSCs in a p–i–n planar device structure. These devices show negligible hysteresis and light soaking, with the background carrier density lowered by more than one order of magnitude compared to a reference cell incorporating an SnF_2 reducing agent. We demonstrate that addition of a very small amount (0.08 M) of layered (2D) tin perovskite in 0.92 M 3D tin perovskite induces superior crystallinity and a well-defined orientation of the 3D $FASnI_3$ grains (hereafter referred to as 2D/3D mixture perovskite). The extended ordering and packing of crystal planes improves the robustness and integrity of the perovskite structure and helps to suppress the formation of tin vacancies and therefore the background carrier density. The high degree of crystallinity and the preferential crystal orientation are fundamental for the improved solar cell performance. The champion reference solar cell gives a PCE of about 6%, i.e., 50% inferior to the record device fabricated with 2D/3D perovskite, due to the high leakage current and severe trap-assisted recombination caused by the high p-doping (10^{17} cm^{-3}) level. Moreover, the 2D/3D-based HPSCs have much higher stability upon exposure to light and ambient conditions due to the enhanced robustness of the perovskite film.

We prepared the tin-based perovskite films via a single-step spin-coating method with antisolvent dripping.[10] The films were subsequently annealed at 65 °C for 20 min. We obtained pristine 3D $FASnI_3$ perovskite films, acting in this work as the reference, from a precursor solution comprising formamidinium iodide (FAI), SnI_2, and SnF_2 with a 1:1:0.1 molar ratio, in a mixture of dimethyl sulfoxide (DMSO) and *N*,*N*-dimethylformamide (DMF).

Our 2D/3D samples were made from a precursor solution containing mixtures of stoichiometric 2-phenylethylammonium iodide (PEAI) xM, FAI $(1 - x)$ M and 1 M SnI_2 and 0.1 M SnF_2, where x is 0, 0.04, 0.08, 0.12, and 0.16, corresponding to stoichiometric $FASnI_3$, $PEA_2FA_{49}Sn_{50}I_{151}$ ($n = 50$), $PEA_2FA_{24}Sn_{25}I_{76}$ ($n = 25$), $PEA_2FA_{15}Sn_{16}I_{49}$ ($n = 16$), and $PEA_2FA_{11}Sn_{12}I_{37}$ ($n = 12$). In our case, the PEA^+ content in the perovskite film is much lower than what reported in previous works. In the following section, we show that the 2D/3D samples are most probably the mixtures of 2D materials and 3D materials rather than a stoichiometric pure phase as shown here.

Figure S1a (Supporting Information) shows X-ray diffraction (XRD) patterns of the different films. The reference $FASnI_3$ film shows five dominant diffraction peaks at angles of 14.0°, 24.4°, 28.22°, 31.65°, 40.37° assigned to the crystallographic planes (100), (120)/(102), (200), (122), (222), respectively. This diffraction pattern is in agreement with previous reports[13] and is consistent with the orthorhombic (*Amm*2) crystal structure of $FASnI_3$, the presence of all the above peaks indicating that the reference film is composed of grains with random orientations. The 2D/3D perovskite films all exhibit the (100) and (200) peaks at angles of 14.0° and 28.22°, as well as a weaker peak at 42.9° assigned to the (300) plane, indicating the same orthorhombic 3D crystal structure as the reference film (see **Figure 1**a). However, the suppression of the 120/102, 122 and 222 peaks together with the enhanced *h*00 peak intensities suggests preferential crystallization with (*h*00) planes parallel to the film surface. This observation is further confirmed by the grazing incidence X-ray scattering data discussed below. The 100 peak

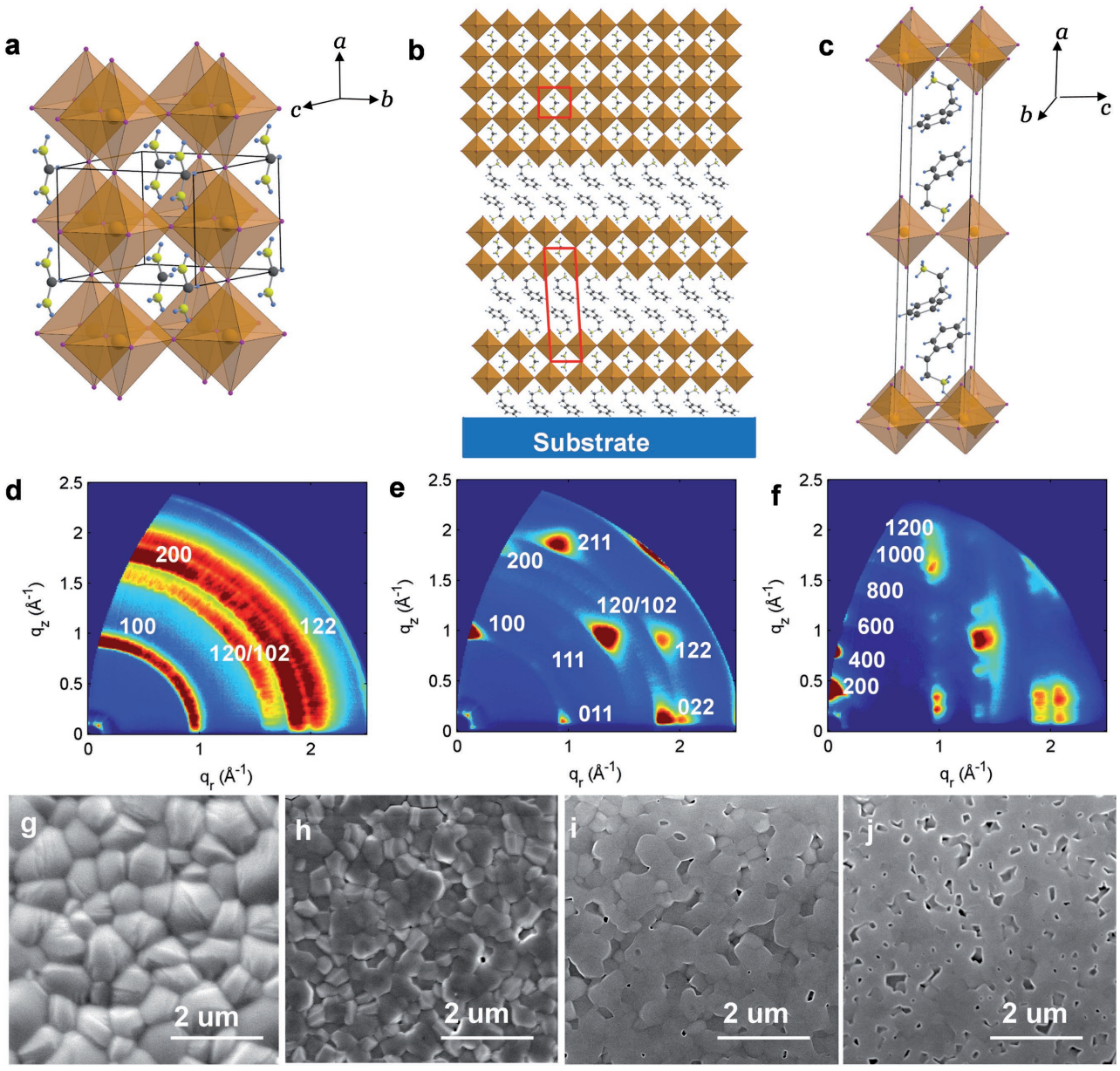

Figure 1. Crystal structure and morphology. Schematic crystal structure of a) 3D reference $FASnI_3$, b) 2D/3D mixture (2D 0.08 M), with the unit cells of each component outlined in red, and c) 2D PEA_2SnI_4. Respective GIWAXS images of samples annealed at 65 °C recorded at an incident angle of 0.25°: d) 3D reference, e) 2D/3D mixture, and f) 2D film. g–j) SEM images of $FASnI_3$ films with different 2D Sn perovskite concentrations (0, 0.08; 0.012, 0.16 M).

of the $FASnI_3$ film with 2D/3D perovskite (0.08 M) is about 40 times more intense than for the reference film (Figure S1b, Supporting Information), with a decreased full-width at half-maximum (FWHM). These data indicate significantly improved crystallinity and more perfect packing of the (100) and (200) planes upon incorporation of PEAI into the $FASnI_3$ film.

In addition, several very weak peaks (magnified 100 times in Figure S1a in the Supporting Information to make them observable) appear at lower 2θ values (<12°). These new peaks do not belong to either SnI_2 or SnF_2 (see Figure S1c in the Supporting Information). Instead, they may indicate formation of a layered tin perovskite (for the probable structure, see Figure 1b). The low diffraction intensity indicates a limited proportion of 2D tin perovskite in the 3D matrix of $FASnI_3$. Figure S1d (Supporting Information) shows the XRD pattern of the pure 2D material (PEA_2SnI_4), which shows strongly preferential crystallization with (h00) planes parallel to the film surface. The a-axis periodicity of ~32 Å is in agreement with the monoclinic structure (space group $C2/m$) reported by Papavassiliou et al.[28] However, the first peak in the XRD pattern of the 2D/3D sample (0.08 M) at $2\theta = 3.8°$ indicates an a-axis of ~23 Å. In the reported PEA_2SnI_4 structure, a double layer of PEA molecules occupies approximately 10.0 Å in the a-direction, whereas a single layer of SnI_6 octahedra in both PEA_2SnI_4 and $FASnI_3$ occupies

6.3–6.4 Å. Therefore, we speculate that the part of the 2D/3D film (0.08 M) that gives rise to the weak diffraction peaks in Figure S1a in the Supporting Information comprises double layers of SnI_6 octahedra separated by double layers of PEA molecules, as shown schematically in Figure 1b.

We further assessed the effects of adding a small amount of 2D perovskite and of thermal annealing on the structure and orientation of the $FASnI_3$ crystals with respect to the substrate using grazing incidence wide-angle X-ray scattering (GIWAXS). Figure 1d–f shows the GIWAXS patterns of the pure 3D, 2D/3D mixture and pure 2D perovskite films (annealed at 65 °C) recorded using an incident angle of 0.25°. The reference 3D film exhibits Debye–Scherrer-like rings whose positions correspond to those of the dominant peaks in the XRD pattern. The rings actually consist of many isotropically distributed spots, indicating significant randomness in the orientations of the grains within the polycrystalline $FASnI_3$ film. In contrast, the 2D/3D film (0.08 M) exhibits Bragg spots located around the same rings, indicating a strongly textured film morphology with preferential orientation of the grains with respect to the substrate. All the Bragg spots can be indexed using an orthorhombic structure in agreement with the XRD data, confirming that the crystal structure of the $FASnI_3$ perovskite in the 2D/3D mixed film is the same as that of the reference 3D material. The location of the 100 and 200 Bragg spots along the q_z direction indicates that the grains orient preferentially with (h00) planes parallel to the substrate, i.e., the a-axis is oriented perpendicular to the substrate. The structure and orientation of the $FASnI_3$ grains is homogeneous throughout the entire film thickness, as GIWAXS patterns recorded using an incident angle of 2° and shown in Figure S2a–c in the Supporting Information (full X-ray penetration of the film) are similar to those recorded at an incident angle of 0.25° (low X-ray penetration depth). Note that two weak diffraction peaks originating from the 2D material become visible only when full penetration of the film by the X-rays is achieved (Figure S2b, Supporting Information), suggesting that the 2D material is mostly located in the proximity of the substrate. The positions of these peaks are in agreement with the two lowest angle peaks in the XRD data. In order to understand whether the thermal treatment at 65 °C affects the structure, GIWAXS images were also recorded for the same set of samples without any thermal annealing (Figure S3, Supporting Information); no significant changes were observed. This implies that the alignment of the SnI_6 octahedra parallel to the substrate is thermodynamically stable. This is an important result as low-temperature processing is fundamental to reduce trap states in the $FASnI_3$ films, especially if one considers the low formation energy of tin vacancies and Sn^{4+}.

The Pb-based 2D perovskite $BA_2MA_3Pb_4I_{13}$, which contains another large organic cation n-butylammonium, forms randomly oriented grains at room temperature and hot casting of the film is necessary to obtain high crystallinity and grains oriented with the layer stacking direction parallel to the film surface.[25] The host casting method is unfavorable for tin-based HPSCs because the high temperature may induce a high density of tin vacancies in the perovskite film. Therefore, our finding is very important as it demonstrates that a very small amount of 2D perovskite inserted into the 3D material is able to induce a highly uniform orientation of the 3D $FASnI_3$ grains at room temperature.

In summary, the 2D tin perovskite functions as a seed layer to induce large-scale crystallization and orientation of the 3D $FASnI_3$ grains (see Figure 1b). The strong tendency of the 2D perovskite to form highly ordered, aligned structures is confirmed by GIWAXS patterns of the pure PEA_2SnI_4 films (Figure 1f; Figure S3c,f in the Supporting Information). The 2D structure could be indexed according to the reported monoclinic unit cell with an a-axis of 32 Å, highly oriented perpendicular to the substrate.[28] We speculate that the organic PEA^+ cations are oriented perpendicularly to the substrate, and the van der Waals interactions of the benzene ring between the interdigitate PEA^+ cations may facilitate self-assembly of the inorganic SnI_6 layers parallel to the substrate, inducing strong orientation and crystallization of the 2D PEA_2SnI_4.

Figure 1g–j shows scanning electron microscopy (SEM) images of the different perovskite films. The reference film has compact morphology with very few pinholes. The $FASnI_3$ grains range from 0.5 to 2 μm and pack together irregularly with rather sharp grain boundaries. Previous work has shown that grain boundaries in lead perovskite films have high concentrations of structural defects such as dangling bonds or vacancies.[29–31] Therefore, grain boundaries function as trap centers for nonradiative recombination. Moreover, they give rise to energy disorder which is an obstacle for charge transport.[32–34] This may also apply to the case of $FASnI_3$ films, in which the tin vacancies are the dominant defects due to their low formation energy.[7,8] The addition of very small amounts of 2D perovskite seems to fuse the $FASnI_3$ grains together and blurs the grain boundaries. This observation is consistent with the improved crystallinity and larger grains indicated by the XRD patterns of the 2D/3D films. However, when the concentration of 2D perovskite increases up to 0.16 M, many pinholes appear in the $FASnI_3$ film, making the morphology far from ideal for the fabrication of solar cells.

To test the effects of the morphological and crystallographic changes in our $FASnI_3$ films on solar cell performance, we implemented them in devices using structures of the type ITO/poly(3,4-ethylenedioxythiophene):polystyrene sulfonate (PEDOT:PSS)/$FASnI_3$/C_{60} + 2,9-dimethyl-4,7-diphenyl-1,10-phenanthroline (BCP)/Al as depicted in **Figure 2**.[16] We chose C_{60} as it produces not only a more uniform and dense electron transport layer but also avoids the need for solvents.

For the fabrication of the reference cell based on 3D $FASnI_3$, we used SnF_2 as a reducing agent to reduce the background carrier density. The reference device has an optimum PCE when the concentration of SnF_2 is 0.1 M and beyond this concentration the device performance deteriorates (Figure S4, Supporting Information). This is because the excess SnF_2 forms aggregates in the $FASnI_3$ film as indicated by previous studies. We further investigated the effect of thermal annealing on the device performance. Optimum performance was obtained when the active layer was annealed at 65 °C (Figure S5, Supporting Information). The performance dropped significantly at higher annealing temperatures, most probably due to the formation of tin vacancies. This again highlights the importance of depositing high-quality $FASnI_3$ films at low temperature for efficient tin-based HPSCs.

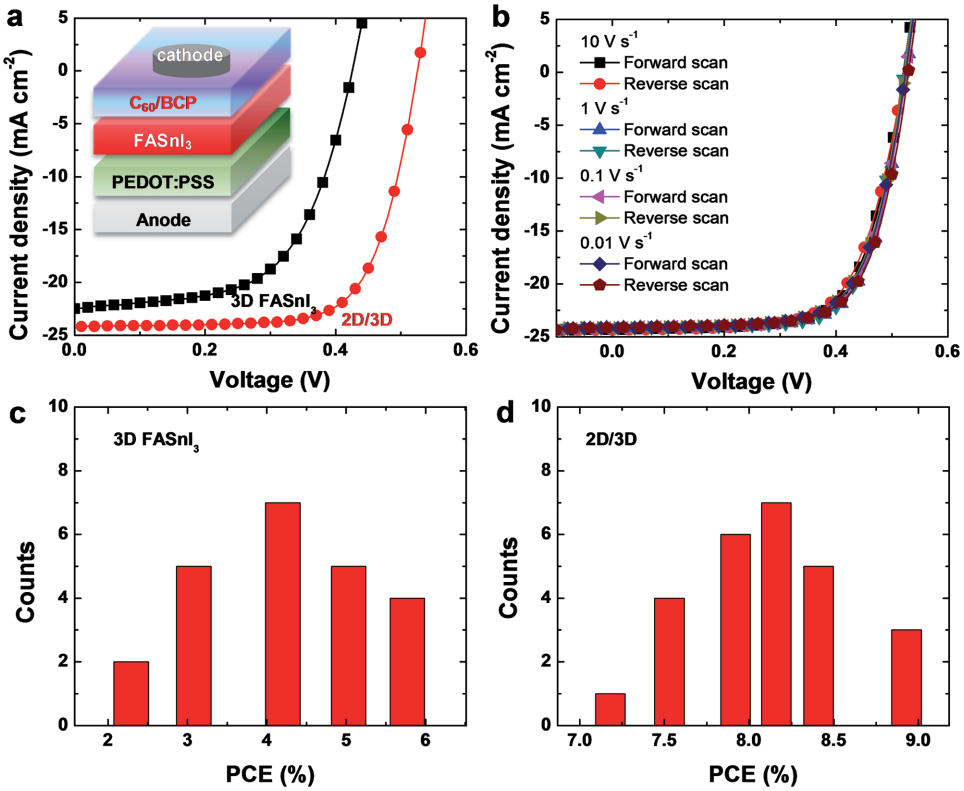

Figure 2. Device structure and characterization. a) *J–V* curves under one sun AM 1.5 G condition for the champion devices containing pure 3D and 2D (0.008 M)/3D perovskite (the inset shows the device structure), b) forward and reverse sweeps of the *J–V* characteristics of the champion 2D/3D perovskite cell measured at different rates, c) histogram of the reference cell reproducibility, and d) of the 2D/3D perovskite devices.

Figure 2a shows the current density (*J*)–voltage (*V*) characteristics under one sun illumination of the best performing reference cell, displaying a V_{OC} of 0.458, a J_{sc} of 22.5 mA cm^{-2}, fill factor (FF) of 0.58 and PCE of 6.0%. We list all the device parameters in **Table 1**. Figure 2c shows the distribution of PCE for the reference cells; the broad variation indicates poor reproducibility over the 20 fabricated devices.

We used the same experimental conditions to fabricate devices with 2D/3D films where PEAI was added to the active layer with different concentrations (Figure S6 in the Supporting Information shows the corresponding *J–V* curves). We obtained the best performing devices with a 0.08 M concentration of 2D perovskite in the $FASnI_3$ film, and we observed a significant drop in performance for higher concentrations of 2D perovskite. This is because the pin holes in the perovskite active layer (see Figure 1j) give rise to shunt paths and direct contact between the cathode and anode, with consequent high leakage current (see Figure S7 in the Supporting Information).

Table 1. Figures of merit for devices with 3D tin perovskite and 2D/3D tin perovskite layers under one sun condition.

Device	V_{OC} [V]	J_{SC} [mA cm^{-2}]	FF	PCE [%]
3D	0.458	22.5	0.58	6.0
2D/3D	0.525	24.1	0.71	9.0

Figure 2a shows the *J–V* characteristics of the best performing device with the 2D/3D film and a comparison with the best reference cell. The 2D/3D device shows a V_{OC} of 0.525 V, a J_{SC} of 24.1 mA cm^{-2} and an FF of 0.71 resulting in a PCE of 9.0%. It is important to note that this is the highest FF and PCE reported so far for all-tin-based perovskite solar cells. Moreover, the *J–V* curves of these solar cells are identical for forward and reverse scans and different sweeping rates (negligible *JV* hysteresis), as shown in Figure 2b. We also point out that this device shows no obvious light-soaking effect, which is confirmed by the fast saturation of the steady state photoluminescence (PL) upon photoexcitation with a 400 nm laser (Figure S8, Supporting Information). The absence of hysteresis and light-soaking effects in these devices is very important, as it represents a sign of their reliability. These phenomena often affect Pb-based HPSCs and render the device performance unreliable.[5,35,36] To further confirm our observations, we independently tested the steady state PCE of the device using 2D/3D mixture (see Figure S9 in the Supporting Information). The 2D/3D-based device from a different batch with a PCE of 8.8% (from *J–V* measurement) has a very similar steady state PCE of 8.5%, confirming the reliable device performance. The PCE statistics (Figure 2d) of more than 20 devices demonstrates the small variation and good reproducibility of our 2D/3D devices compared to the reference devices.

The device containing the 2D/3D film shows substantially improved performance parameters with respect to the 3D

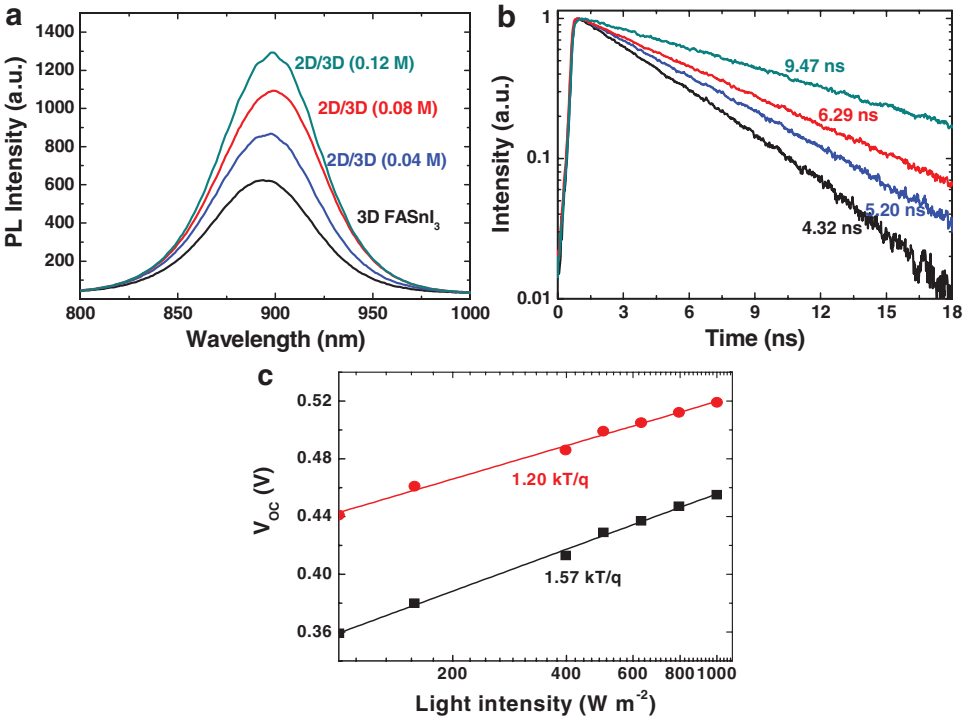

Figure 3. Spectroscopy and light intensity dependent characterization. a) Steady state PL and b) time-resolved PL for perovskite films with different concentrations of 2D perovskite (black line for 0 M, blue line for 0.04 M, red line for 0.08 M, and green line for 0.12 M). c) Light intensity dependence of V_{OC} for devices with 2D (0.08 M)/3D perovskite (red) and 3D perovskite (black).

reference: 15% higher V_{OC}, 7% higher J_{SC}, 20% higher FF and 50% higher PCE. The integrated J_{SC} values (23.8 mA cm^{-2} for 2D/3D-based device and 22.2 mA cm^{-2} for 3D-based device) from the external quantum efficiency of incident photons to electrons (EQE) measurement confirm the value of the photocurrent density measured using the *J*–*V* characteristics (Figure S10, Supporting Information).

The 2D/3D film (0.08 M) has the same absorption onset as the 3D film (see Figure S11a in the Supporting Information), but it has higher optical constants (extinction coefficient and refractive index) than the 3D film due to its superior crystallinity (Figure S11b, Supporting Information). Optical simulations performed using transfer matrix formalism provide photocurrent generation profiles for both devices, showing similar theoretical photocurrent densities and excluding optical absorption as the dominant factor for the improvement in the experimental J_{SC} of the device with the 2D/3D film (Figure S11c, Supporting Information).

In order to gain deeper insight into the 50% improvement in device performance with the 2D/3D film, we performed steady-state and time-resolved PL measurements on the different $FASnI_3$ films. In **Figure 3**a, we observe that all the $FASnI_3$ films have emission peaks around 895 nm. The reference sample displays the lowest emission intensity, implying higher nonradiative trap-assisted recombination losses of charge carriers. Due to the capture of free carriers by the defect sites, the photogenerated carriers decay rather fast and the emission lifetime is as short as 4.1 ns. A consequence of this short lifetime is that the charge carriers can only diffuse a short distance and have a high probability of recombination with the opposite charge carriers before they reach the respective electrodes. Therefore, the inefficient charge collection efficiency leads to lower J_{SC} and FF in the reference device. The reference $FASnI_3$ films are affected by large fluctuations in the number of defects due to the randomly packed grains or sensitivity to the atmosphere in the N_2-filled glove box. As a result, the reference cell shows a broad distribution of PCEs.

The 2D/3D film has significantly improved emission intensity and lifetime (up to 9.47 ns), indicating much lower trap density than the pure 3D film. These results confirm that the extended ordering of the crystal planes and the reduced number of grain boundaries help to reduce the trap density in the perovskite film. As mentioned earlier, the highly ordered and oriented crystal planes parallel to the substrate may form fast transport pathways for the charge carriers in the device. In this case, the long-lived charge carriers can be transported efficiently to the respective electrodes before recombination occurs, which leads to the improved FF and J_{SC} in the device. Because of the negligible hysteresis and light soaking, we further performed the *J*–*V* measurements under various light intensities with an interval of 5–10 s between the *J*–*V* sweeps. Figure 3c shows that the device containing the 2D/3D film exhibits a lower slope of V_{OC} versus semilogarithmic light intensity, further confirming that trap-assisted recombination losses are suppressed compared to the reference device. Previous studies indicate that the severe trap-assisted recombination loss of charge carriers is one of the main reasons for the loss in V_{OC} of the HPSCs.[5,28,29] Therefore, the device based on the 2D/3D tin perovskite exhibits higher V_{OC} than the reference device.

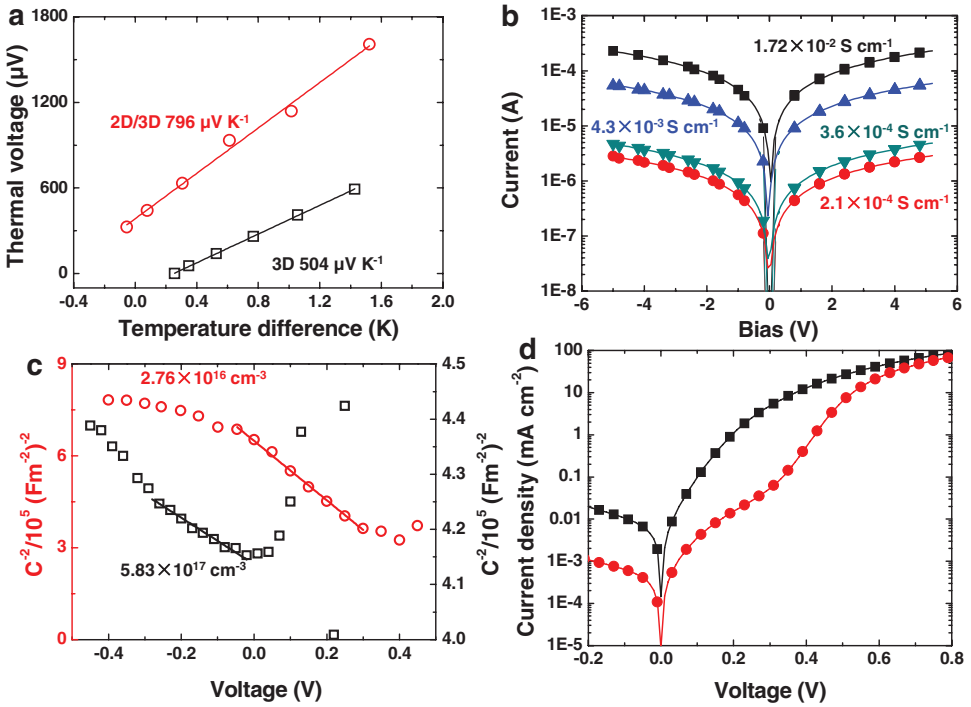

Figure 4. Electrical characteristics of perovskite films. a) Thermal voltage as a function of temperature gradient for the pristine $FASnI_3$ film. b) Two-point probe electrical conductivity for $FASnI_3$ films with different amounts of 2D tin perovskite (black line for 0, blue line for 0.04 M, red line for 0.08 M and green line for 0.12 M). c) C^{-2} as a function of bias voltage. d) *J–V* curves under dark condition for devices with 2D (0.08 M)/3D perovskite (red line) and 3D perovskite (black line) layers.

Figure 4a shows the thermal voltage versus temperature gradient for the 3D and 2D/3D perovskite films, which demonstrate a positive Seebeck coefficient (p-type) of 504 and 796 μV K^{-1} confirming that holes are the dominant carriers. The larger Seebeck coefficient of 2D/3D sample is a signature of lower charge carrier density compared to the pure 3D sample. To further probe how the 2D perovskite influences the p-doping level in $FASnI_3$ films, we carried out electrical conductivity measurements. Figure 4b shows that the reference film has the highest conductivity (1.72×10^{-2} S cm^{-1}) of all the samples. This is a further indication of self-doping by the large density of background holes generated by tin vacancies and oxidized species (Sn^{4+}) and highlights the limitation of SnF_2 as a reducing agent in suppressing these defects. As discussed earlier, the high p-doping level leads to high leakage current and device shorts. The 2D/3D perovskite films have much lower electrical conductivity, indicating de-doping of the $FASnI_3$ film and reduction of the background charge carrier density. We believe that this is related to the increased crystallinity and smaller number of grain boundaries in the 2D/3D perovskite film, which lowers the possibility of forming tin vacancies and Sn^{4+}. The 2D/3D perovskite film (0.08 M) exhibits a hole conductivity of 2.1×10^{-4} S cm^{-1}, which is more than two orders of magnitude lower than the reference sample.

Figure 4c shows the variation of the background charge carrier density in the devices containing 3D and 2D/3D perovskite layers obtained from capacitance (*C*)–voltage (*V*) measurements under dark conditions. Using Mott–Schottky analysis

$$C^{-2} = \frac{2}{q\varepsilon_r\varepsilon_0 N}\left(V - V_{fb} - \frac{kT}{q}\right) \quad (1)$$

the background charge carrier density can be obtained from the slope of C^{-2} versus the applied voltage V in the depletion region. The hole carrier density (2.76×10^{16} cm^{-3}) in solar cells with layered tin perovskite is reduced by more than 20 times compared to the reference cell (5.83×10^{17} cm^{-3}), in agreement with the conductivity measurements.

Figure 4d shows the dark *J–V* curves of the devices containing 3D and 2D/3D tin perovskite layers, from which we extracted the shunt resistances (R_P). The reference solar cell has a small R_P (9.7 kΩ cm^2) and suffers significantly from a high leakage current due to the high p-doping level. In contrast, the device with the 2D/3D perovskite layer has a much higher shunt resistance (175 kΩ cm^2) and very good diode behavior, which originates from the low background carrier density. In addition, the improved crystallinity and the highly oriented packing of the crystal planes in the out-of-plane direction favor charge transport and collection in the device. This provides more evidence that the high device performance is correlated with the crystallographic and morphological characteristics of the 2D/3D film. In addition, the highly crystalline and oriented structure of the 2D/3D film is also the reason for the good reproducibility of the device performance.

Beside the efficiency, the stability is equally important for practical applications of perovskite solar cells. We firstly tested the device stability under one sun illumination in an N_2-filled glove box (Figure S12, Supporting Information). During

2 h exposure to the solar light, both the reference and 2D/3D devices show relatively constant V_{OC}. However, the reference device shows considerable degradation of both J_{SC} and FF with time. In contrast, the 2D/3D perovskite device has relatively stable J_{SC} and FF. As a consequence, the efficiency of the reference cell is reduced to 75% of its initial efficiency after 2 h whereas the 2D/3D device does not show any obvious degradation. The improved crystallinity of the perovskite film may enable higher resistance to light illumination and reduce the possibility for formation of the defects in the 2D/3D-based device, leading to enhanced stability.

Furthermore, we tested the stability of the devices (C_{60} 70 nm) without any encapsulation in ambient condition with humidity about 20% (temperature about 20°C) as shown in Figure S13 in the Supporting Information. Between the intervals of the test, the devices were stored in dark condition. The device based on 2D/3D sample shows much higher stability compared to the device using pure 3D sample. After 76 h exposure to air, the device using pure 3D perovskite completely failed, whereas the device using 2D/3D mixture retained 59% of the original PCE. In order to understand the discrepancy in the stability of the devices, we further performed XRD measurements for the perovskite samples stored in nitrogen filled glove box (H_2O < 0.1 ppm, O_2 < 0.1 ppm) and in air (humidity about 70%, temperature 22 °C). Both the 3D and 2D/3D samples do not show obvious decomposition after 6 h in inert atmosphere, whereas the 3D sample undergoes faster chemical degradation than the 2D/3D sample when stored in ambient conditions (Figure S14, Supporting Information). The improved ambient stability of the 2D/3D-based device is probably due to higher resistance to oxygen and moisture as a result of the improved crystallinity and the higher hydrophobicity of the perovskite film.

In conclusion, we have demonstrated all-tin-based HPSCs with efficiencies of up to 9%. The addition of a trace amount of 2D tin perovskite initiates the homogenous growth of highly crystalline and oriented $FASnI_3$ grains at low temperature. The high degree of order has three positive consequences: (i) a reduced number of grain boundaries; (ii) the suppression of tin vacancies or Sn^{4+} and a consequent reduction in background carrier density by more than one order of magnitude compared to pristine $FASnI_3$ films; (iii) a longer lifetime of the charge carriers. Therefore, devices based on a 2D/3D tin perovskite layer benefit from low trap-assisted recombination, low shunt losses of the charge carriers and efficient charge collection. Moreover, the improved crystallinity of the active layer results in more stable HPSCs.

In stark contrast, reference films using only SnF_2 as a reducing agent have a high degree of structural disorder, a high density of sharp grain boundaries and randomly oriented 3D grains. This facilitates the formation of a high density of tin vacancies and causes a high p-doping level. As a consequence, the best reference cell has a PCE of 6%, and suffers from severe trap-assisted recombination and high leakage current.

Finally, by adding trace amount of 2D tin perovskite in $FASnI_3$ we overcome the bottleneck that has long been faced by tin-based HPSCs and demonstrate a way forward to further improve their performance.

Experimental Section

Materials: PEDOT:PSS water dispersion (Clevios VP AI 4083) was acquired from Heraeus. PEAI (>98%) and FAI (>98%) were purchased from TCI EUROPE N.V. SnI_2 (99.999%), SnF_2 (>99%), C_{60} (>99.9%), BCP (99.99%), DMF (99.8%), and DMSO (99.8%) were purchased from Sigma Aldrich. All the materials were used as received without further purification.

SEM Measurement: SEM images were recorded in air on an FEI NovaNano SEM 650 with an acceleration voltage of 10 kV.

XRD: XRD patterns (Figure S1, Supporting Information) of the perovskite films were recorded in air (RH about 20%, *T* about 20 °C) on a Bruker D8 Advance X-ray diffractometer with a Cu Kα source (λ = 1.54 Å) and a Lynxeye detector. The perovskite samples were encapsulated by Kapton thin film. The XRD patterns for the stability test (Figure S14, Supporting Information) were performed for the samples aged in glove box and in air with ambient RH about 70% and *T* about 22 °C.

GIWAXS Measurement: GIWAXS measurements were performed using a MINA X-ray scattering instrument built on a Cu rotating anode source (λ = 1.5413 Å). 2D patterns were collected using a Vantec500 detector (1024 × 1024 pixel array with pixel size 136 × 136 µm) located 93 mm away from the sample. The perovskite films were placed in reflection geometry at certain incident angles α_i with respect to the direct beam using a Huber goniometer. GIWAXS patterns were acquired using incident angles from 0.25° to 2° in order to probe the thin film structure at different X-ray penetration depths. For an ideally flat surface, the value of the X-ray penetration depth (i.e., the depth into the material measured along the surface normal where the intensity of X-rays falls to 1/*e* of its value at the surface) depends on the X-ray energy (wavelength λ), the critical angle of total reflection, α_c, and the incident angle, α_i, and can be estimated using the relation: $\Lambda = \frac{\lambda}{4\pi}\sqrt{\frac{2}{(\alpha_i^2-\alpha_c^2)^2+4\beta^2-(\alpha_i^2-\alpha_c^2)}}$, where β is the imaginary part of the complex refractive index of the compound. The estimated X-ray penetration depth is 10 and 40 nm at incident angle of 0.25°, and 350 and 600 nm at incident angle of 2.0° for the pure 3D and 2D perovskites, respectively. For the calculation, the densities of 3.56 and 2.35 g cm^{-3} were used for the pure 3D and 2D perovskites, respectively. The direct beam center position on the detector and the sample-to-detector distance were calibrated using the diffraction rings from standard silver behenate and Al_2O_3 powders. All the necessary corrections for the GIWAXS geometry were applied to the raw patterns using the GIXGUI Matlab toolbox.[37] The reshaped GIWAXS patterns, taking into account the inaccessible part in reciprocal space (wedge-shaped corrected patterns), are presented as a function of the vertical and parallel scattering vectors q_z and q_r. The scattering vector coordinates for the GIWAXS geometry are given by[38]

$$q = \begin{cases} q_x = \frac{2\pi}{\lambda}\left(\cos(2\theta_f)\cos(\alpha_f) - \cos(\alpha_i)\right) \\ q_y = \frac{2\pi}{\lambda}\left(\sin(2\theta_f)\cos(\alpha_f)\right) \\ q_z = \frac{2\pi}{\lambda}\left(\sin(\alpha_i) + \sin(\alpha_f)\right) \end{cases} \quad (2)$$

where $2\theta_f$ is the scattering angle in the horizontal direction and α_f is the exit angle in the vertical direction. The parallel component of the scattering vector is thus calculated as $q_r = \sqrt{q_x^2 + q_y^2}$.

Steady-State and Time-Resolved PL Measurement: Steady-state and time-resolved PL measurements were conducted by exciting the samples with the second harmonic (400 nm) of a mode-locked Ti:Sapphire femtosecond laser (Mira 900, Coherent). The repetition rate of the laser is 76 MHz; a pulse picker was inserted in the optical path to decrease the repetition rate of the laser pulses. The laser power

(0.7 μJ cm^{-2}) was adjusted using neutral density filters. The excitation beam was focused with a 150 mm focal length lens, and the emission was collected and coupled into a spectrometer with a 50 lines mm^{-1} grating. The steady-state PL was recorded with an Image EM CCD camera from Hamamatsu (Hamamatsu, Japan). Time-resolved PL was measured with a Hamamatsu streak camera working in single sweep mode.

Electrical Conductivity, Seebeck Coefficient, and C–V Measurement: For the electrical conductivity measurements, parallel line-shaped Au electrodes with a width (w) of 13 mm and a channel length (L) of 200 μm were deposited on cleaned glass substrates as bottom contacts. Different perovskite films were spin-coated on the patterned glass following the same recipe used for photovoltaic device fabrication. Voltage-sourced two-point conductivity measurements were conducted using a probe station in a N_2 glovebox. The electrical conductivity (σ) was calculated according to the formula $\sigma = (J/V) \times L/(w \times d)$, where d is the thickness of the perovskite films. The Seebeck coefficient was measured with a home-built setup[39] in a vacuum probe station. Temperature steps were imposed across the devices to measure the thermal voltages of perovskite thin films at different temperatures, which were detected by a standard constantan wire (127 μm from Omega, Seebeck coefficient of –39 μV K^{-1}).

The capacitance–voltage (C–V) measurements were conducted under dark condition at a frequency of 10 kHz with an ac drive voltage of 20 mV and DC bias in the range of –0.6 to 0.6 V on a Solarton 1260 impedance gain-phase analyzer.

UV–vis Measurement: UV–vis spectra of the perovskite films were recorded on Shimatzu UV-Vis-NIR spectrophotometer (UV 3600). The perovskite samples were encapsulated with quartz using UV light curing adhesive.

Device Fabrication: ITO glasses were cleaned using an ultra-sonication bath in soap water and rinsed sequentially with de-ionized water, acetone and isopropyl alcohol. A PEDOT:PSS layer was then spin-coated onto the ITO substrates at 4000 rpm for 60 s and dried at 140 °C for 20 min. The coated substrates were then transferred to a nitrogen-filled glove-box. The reference $FASnI_3$ film was spin-coated from a precursor solution comprising 1 M FAI, 1 M SnI_2 and 0.1 M SnF_2 in mixed solvents of DMSO and DMF (1:4 volume ratio) at 4000 rpm for 60 s. Diethyl ether was used as the antisolvent during the spin-coating process. The $FASnI_3$ film was then annealed at 65 °C for 20 min. The 2D/3D tin perovskite films were obtained under the same conditions from solutions containing x M PEAI (x = 0.04, 0.06, 0.08, 0.12, 0.16 M), (1 – x) M FAI, 1 M SnI_2, and 0.1 M SnF_2. Next, 30 nm C_{60}, 6 nm BCP, and 100 nm Al layers were sequentially evaporated on top of the perovskite film under vacuum of $<10^{-6}$ mbar. The J–V curves of the perovskite solar cells were measured at 295 K using a Keithley 2400 source meter under simulated AM 1.5 G solar illumination using a Steuernagel Solar constant 1200 metal halide lamp in a nitrogen-filled glove box. The light intensity was calibrated to be 100 mW cm^{-2} by using a Si reference cell and correcting the spectral mismatch. A shadow mask (0.04 cm^2) was used to exclude lateral contributions beyond the device area.

Supporting Information

Supporting Information is available from the Wiley Online Library or from the author.

Acknowledgements

The authors would like to thank the financial support from European Commission, Marie Curie Actions—Intra-European Fellowships (IEF) "SECQDSC" No. 626852 and European Research Council, ERC Starting Grant "HySPOD" No. 306983. The authors also appreciate the technical supports of A. Kamp and T. Zaharia.

Conflict of Interest

The authors declare no conflict of interest.

Keywords

background charge carrier density, crystallinity, grain boundaries, tin perovskite solar cells, tin vacancies

Received: July 24, 2017
Revised: August 21, 2017
Published online: September 22, 2017

[1] Best efficiency-chart at https://www.nrel.gov/pv/assets/images/efficiency-chart.
[2] R. E. Beal, D. J. Slotcavage, T. Leijtens, A. R. Bowring, R. A. Belisle, W. H. Nguyen, G. F. Burkhard, E. T. Hoke, M. D. McGehee, *J. Phys. Chem. Lett.* **2016**, *7*, 746.
[3] M. Saliba, T. Matsui, J.-Y. Seo, K. Domanski, J.-P. Correa-Baena, M. K. Nazeeruddin, S. M. Zakeeruddin, W. Tress, A. Abate, A. Hagfeldt, M. Grätzel, *Energy Environ. Sci.* **2016**, *9*, 1989.
[4] A. Mei, X. Li, L. Liu, Z. Ku, T. Liu, Y. Rong, M. Xu, M. Hu, J. Chen, Y. Yang, M. Grätzel, H. Han, *Science* **2014**, *345*, 295.
[5] S. Shao, M. Abdu-Aguye, L. Qiu, L.-H. Lai, J. Liu, S. Adjokatse, F. Jahani, M. E. Kamminga, G. H. ten Brink, T. T. M. Palstra, B. J. Kooi, J. C. Hummelen, M. A. Loi, *Energy Environ. Sci.* **2016**, *9*, 2444.
[6] I. Chung, B. Lee, J. He, R. P. H. Chang, M. G. Kantatzidis, *Nature* **2012**, *485*, 486.
[7] H. Yu, H. Lu, F. Xie, S. Zhou, N. Zhao, *Adv. Funct. Mater.* **2016**, *26*, 1411.
[8] C. Yu, Z. Chen, J. J. Wang, W. Pfenninger, N. Vockic, J. T. Kenney, K. Shum, *J. Appl. Phys.* **2011**, *110*, 063526.
[9] Z. Chen, C. Yu, K. Shum, J. J. Wang, W. Pfenninger, N. Vockic, J. Midgley, J. T. Kenney, *J. Lumin.* **2012**, *132*, 345.
[10] H.-J. Du, W.-C. Wang, J.-Z. Zhu, *Chin. Phys. B* **2016**, *25*, 1.
[11] M. Konstantakou, T. Stergiopoulos, *J. Mater. Chem. A* **2017**, *5*, 11518.
[12] N. K. Noel, S. D. Stranks, A. Abate, C. Wehrenfennig, S. Guarnera, A.-A. Haghighirad, A. Sadhanala, G. E. Eperon, S. K. Pathak, M. B. Johnston, A. Petrozza, L. M. Herz, H. J. Snaith, *Energy Environ. Sci.* **2014**, *7*, 3061.
[13] F. Hao, C. C. Stoumpos, D. H. Cao, R. P. H. Chang, M. G. Kanatzidis, *Nat. Photonics* **2014**, *8*, 489.
[14] M. H. Kumar, S. Dharani, W. L. Leong, P. P. Boix, R. R. Prabhakar, T. Baikie, C. Shi, H. Ding, R. Ramesh, M. Asta, M. Graetzel, S. G. Mhaisalkar, N. Mathews, *Adv. Mater.* **2014**, *26*, 7122.
[15] S. J. Lee, S. S. Shin, Y. C. Kim, D. Kim, T. K. Ahn, J. H. Noh, J. Seo, S. Il Seok, *J. Am. Chem. Soc.* **2016**, *138*, 3974.
[16] W. Liao, D. Zhao, Y. Yu, C. R. Grice, C. Wang, A. J. Cimardi, P. Schulz, W. Meng, K. Zhu, R.-G. Xiong, Y. Yan, *Adv. Mater.* **2016**, *28*, 9333.
[17] D. Moghe, L. Wang, C. J. Traverse, A. Redoute, M. Sponseller, P. R. Brown, V. Bulovic, R. R. Lunt, *Nano Energy* **2016**, *28*, 469.
[18] N. Wang, Y. Zhou, M.-G. Ju, H. F. Garces, T. Ding, S. Pang, X. C. Zeng, N. P. Padture, X. W. Sun, *Adv. Energy Mater.* **2016**, *6*, 1601130.
[19] T. B. Song, T. Yokoyama, C. C. Stoumpos, J. Logsdon, D. H. Cao, M. R. Wasoelewski, S. Aramsk, M. G. Kanatzidis, *J. Am. Chem. Soc.* **2017**, *139*, 836.

[20] K. P. Marshall, R. I. Walton, R. A. Hatton, *J. Mater. Chem. A* **2015**, *3*, 1163.
[21] K. P. Marshall, M. Walker, R. I. Walton, R. A. Hatton, *Nat. Energy* **2016**, *1*, 16178.
[22] Z. Zhao, F. Gu, Y. Li, W. Sun, S. Ye, H. Rao, Z. Liu, Z. Bian, C. Huang, *Adv. Sci.* https://doi.org/10.1002/advs.201700204.
[23] I. C. Smith, E. T. Hoke, D. Solis-Ibarra, M. D. McGehee, H. I. Karunadasa, *Angew. Chem.* **2014**, *126*, 11414.
[24] D. H. Cao, C. C. Stoumpos, O. K. Farha, J. T. Hupp, M. G. Kanatzidis, *J. Am. Chem. Soc.* **2015**, *137*, 7843.
[25] H. Tsai, W. Nie, J.-C. Blancon, C. C. Stoumpos, R. Asadpour, B. Harutyunyan, A. J. Neukirch, R. Verduzco, J. J. Crochet, S. Tretiak, L. Pedesseau, J. Even, M. A. Alam, G. Gupta, J. Lou, P. M. Ajayan, M. J. Bedzyk, M. G. Kanatzidis, A. D. Mohite, *Nature* **2016**, *536*, 312.
[26] D. H. Cao, C. C. Stoumpos, T. Yokoyama, J. L. Logsdon, T.-B. Song, O. K. Farha, M. R. Wasielewski, J. T. Hupp, M. G. Kanatzidis, *ACS Energy Lett.* **2017**, *2*, 982.
[27] Y. Liao, H. Liu, W. Zhou, D. Yang, Y. Shang, Z. Shi, B. Li, X. Jiang, L. Zhang, L. N. Quan, R. Quintero-Bermudez, B. R. Sutherland, Q. Mi, E. H. Sargent, Z. Ning, *J. Am. Chem. Soc.* **2017**, *139*, 6693.
[28] G. C. Papavassiliou, I. B. Koutselas, A. Terzis, M.-H. Whangbo, *Solid State Commun.* **1994**, *91*, 695.
[29] S. Shao, M. Abdu-Aguye, T. S. Sherkar, H.-H. Fang, S. Adjokatse, G. ten Brink, B. J. Kooi, L. J. A. Koster, M. A. Loi, *Adv. Funct. Mater.* **2016**, *26*, 8094.
[30] X. Jia, L. Zhang, Q. Luo, H. Lu, X. Li, Z. Xie, Y. Yang, Y.-Q. Li, X. Liu, C.-Q. Ma, *ACS Appl. Mater. Interfaces* **2016**, *8*, 18410.
[31] W. Wang, J. Yuan, G. Shi, X. Zhu, S. Shi, Z. Liu, L. Han, H.-Q. Wang, W. Ma, *ACS Appl. Mater. Interfaces* **2015**, *7*, 3994.
[32] A. Walsh, D. O. Scanlon, S. Chen, X. G. Gong, S.-H. Wei, *Angew. Chem., Int. Ed.* **2014**, *54*, 1791.
[33] J. S. Yun, J. Seidel, J. Kim, A. M. Soufiani, S. Huang, J. Lau, N. J. Jeon, S. SeokII, M. A. Green, A. Ho-Baillie, *Adv. Energy Mater.* **2016**, *6*, 1600330.
[34] P. Xu, S. Chen, H.-J. Xiang, X.-G. Gong, S.-H. Wei, *Chem. Mater.* **2014**, *26*, 6068.
[35] E. L. Unger, E. T. Hoke, C. D. Bailie, W. H. Nguyen, A. R. Bowring, T. Heumüller, M. G. Christoforo, M. D. McGehee, *Energy Environ. Sci.* **2014**, *7*, 3690.
[36] W. Tress, N. Marinova, T. Moehl, S. M. Zakeeruddin, M. K. Nazeeruddin, M. Grätzel, *Energy Environ. Sci.* **2015**, *8*, 995.
[37] J. Zhang, *J. App. Cryst.* **2015**, *48*, 917.
[38] G. Renaud, R. Lazzari, F. Leroy, *Surf. Sci. Rep.* **2009**, *64*, 255.
[39] J. Liu, L. Qiu, R. Alessandri, X. Qiu, W. Talsma, G. Ye, M. A. Loi, R. C. Chiechi, J. C. Hummelen, L. J. A. Koster, unpublished.